Title

Volcanic tremor and plume height hysteresis from Pavlof Volcano, Alaska

Journal

Science, 355(6320)

ISSN

0036-8075

Authors

Fee, David
Haney, Matthew M
Matoza, Robin S
et al.

Publication Date

2017-01-06

DOI

10.1126/science.aah6108

Title: Volcanic tremor and plume height hysteresis from Pavlof Volcano, Alaska

Authors: David Fee[1], Matthew M. Haney[2], Robin S. Matoza[3], Peter Cervelli[2], Alexandra M. Iezzi[1], Alexa R. Van Eaton[4], David J. Schneider[2]

Affiliations:

[1]Alaska Volcano Observatory, Wilson Alaska Technical Center, Geophysical Institute, University of Alaska Fairbanks, 903 Koyukuk Drive, Fairbanks, AK 99775

[2]Alaska Volcano Observatory, U.S. Geological Survey, 4230 University Drive, Anchorage, AK 99508, USA

[3]Department of Earth Science and Earth Research Institute, University of California, 1006 Webb Hall, Santa Barbara, Santa Barbara, CA 93106

[4]Cascades Volcano Observatory, U.S. Geological Survey, 4230 University Drive, Anchorage, AK 99508, USA

Abstract: The March 2016 eruption of Pavlof Volcano, Alaska produced ash plumes that canceled over 100 flights in North America. The eruption produced strong tremor recorded by seismic and remote low-frequency acoustic (infrasound) stations, including the EarthScope Transportable Array. The relationship between the tremor amplitudes and plume height changes considerably between the waxing and waning portions of the eruption. Similar hysteresis has been observed between seismic river noise and discharge during storms, suggesting flow and erosional processes in both rivers and volcanoes can produce irreversible structural changes detectable in geophysical data. We propose that the time-varying relationship at Pavlof arose from changes in the tremor source related to volcanic vent erosion. This relationship may improve estimates of volcanic emissions and characterization of eruption size and intensity.

One Sentence Summary: The relationship between volcanic tremor and plume height changes during the waxing and waning portions of the eruption.

Main Text:

There are a number of well-documented challenges in monitoring volcanic eruptions and their associated hazards (e.g. *1, 2*). Observatories typically rely on local seismic networks and satellites to make critical decisions about eruption size and intensity. However, seismic networks can be sparse and difficult to maintain, particularly

at remote volcanoes like those in the Aleutian Islands. Satellites often have limited spatial and temporal resolution and may be inhibited by cloud cover. Other remote geophysical methods, such as infrasound (low frequency acoustic) arrays, can provide unique and detailed information on eruption processes (e.g. *3*), but may also be part of a sparse network and have limited signal-to-noise ratio (SNR) and latency due to the propagation distance. It is therefore a priority to integrate multiple observations to assess the eruptive hazards during crisis response. However, we currently lack the ability to quantitatively link seismo-acoustic observations to the intensity of ash emissions.

Seismic and infrasonic volcanic tremor is the continuous vibration of the ground and air, respectively, from a volcano. The origin of volcanic tremor is a subject of active research, with attempts to understand its relation to fluid transport in the solid earth and atmosphere (e.g. *3, 4*). Volcanic tremor during a sustained eruption is termed eruption tremor. Models of seismic eruption tremor include a downward vertical force on the Earth in response to volcanic jet thrust (*5*), erosion of the volcanic conduit and vent (*6*), and chaotic wagging of a magma column (*7*). Infrasonic tremor during eruptions has been compared to the noise from high velocity, turbulent jet flows (*8*) and longer period oscillations are modeled as the result of the emplacement and oscillation of the plume (*9*). However, these models do not explain all features of eruption tremor, and do not currently provide accurate estimates of critical eruption source parameters, such as mass flux and plume height. Similarly, although there is general agreement between tremor characteristics (such as amplitude) with parameters like plume height (e.g. *10, 11, 12*), sizable deviations are possible. Improved understanding of the volcanic tremor source is critical for real-time eruption characterization and hazard mitigation.

The eruption of Pavlof Volcano, Alaska in March 2016 demonstrates the need for accurate tremor models and improved links to eruption source parameters. The eruption occurred in a remote area on the Alaska Peninsula (Fig. 1A) with no warning or precursory seismicity. A sustained ash plume was emitted for ~40 hours that grew steadily in height from 5-9 km above sea level, remained at this level for hours, and then diminished. The plume extended more than 600 km to the northeast over Alaska and eventually to Canada, caused the cancellation of ~100 commercial airline flights, and produced minor ashfall in communities downwind up to 450 km.

We analyzed local seismic and remote infrasound data and compared them to observations of ash plume height. The Alaska Volcano Observatory (AVO) operates a limited local seismic network of six short-period seismometers on Pavlof Volcano (Fig. 1B). We examined seismic data from station PS1A, as it stayed on-scale and operational during the entire eruption. The University of Alaska Fairbanks operates infrasound arrays at 460 km (Dillingham, DLL) and 1300 km (Fairbanks, IS53), which recorded the eruption. The DLL array recorded the eruption with high SNR and was selected for comparison (*13*). Seismic and infrasonic amplitudes strongly correlated during the eruption. However, they showed a marked hysteresis with the ash plume height during the waxing and waning portions of the eruption. This was unexpected because existing models predict that the plume height scales with the $1/4^{th}$ power of mass flux (*14,15*). We propose that changes in the vent and tremor source produced the time-dependent relationship between tremor and plume height, and hence mass flux.

The recent deployment of the EarthScope Transportable Array (TA) in Alaska presents a unique opportunity to use an advanced continental-scale geophysical network

for volcano monitoring and characterization, with numerous co-located seismic and acoustic sensors deployed over a large region. At the time of the eruption, 45 TA stations were operational in Alaska (Fig. 1). We used seismic-acoustic coherence analysis to find acoustic waves on the infrasound channel and ground-coupled airwaves on the vertical seismic channel (Fig. 2) (*16, 17*). This technique was appropriate due to the low SNR expected at this distance and the prevalence of ground-coupled acoustic waves in seismic data (*18*). Four TA stations recorded acoustic waves from the eruption (Fig. 1A), with station O19K (695 km) having the highest coherence. Figure 2 shows the 0.8–5 Hz filtered seismic and infrasonic data for O19K, along with the windowed coherence as a function of time. High coherence lasts for >14 hours, indicating the recording of acoustic waves from Pavlof. We applied coherence-weighting to improve the infrasound waveform SNR (*13*). The resultant filtered waveform (Fig. 2D) has improved signal and frequency characteristics that correspond to times of high seismic-acoustic coherence. The filtered seismic data from local station PS1A compares favorably with the periods of high coherence (Fig. 2E). This represents a unique signal detected on the TA, and suggests future eruption studies and monitoring using TA data.

Local seismic and remote infrasound data provide a detailed chronology for the 39 hours of eruption (Fig. 3A). The Pavlof eruption began with an abrupt increase in seismic tremor at ~23:55 on 27 March. Seismic and infrasonic amplitudes rose steadily until 28 March 04:00, when there was a sharp increase in amplitude. Tremor amplitudes stabilized between 05:00-16:45, followed by a somewhat erratic decline to low levels. A low frequency seismic event also occurred near the summit at ~16:45. Overall there is excellent agreement between the seismic and infrasonic amplitudes and their temporal

evolution. O19K has a similar evolution; however, the trend is not as clear due to the lower SNR.

We estimated the volcanic plume height using satellite imagery and a Federal Aviation Administration webcam located ~60 km southwest of Pavlof (Fig. S1). Webcam images were available during daylight hours at 10 min intervals, with an accuracy of ~300 m. Satellite-based plume heights were obtained using the plume top temperature method (*14*). Plume heights show a gradual rise, leveling off, and then decline during the eruption (Fig. 3B). The first plume observation is 28 March 00:51 at 4.8 km. The plume height gradually rises to 7.6 km before nightfall. Satellite observations show plumes between 7.5–8 km from 08:14–14:37. Webcam observations resume at 15:14, showing heights of ~8 km until they rapidly decline from 19:35–21:05. A weak but sustained plume stays attached to the vent until at least 05:00 on March 29th.

Comparison of the tremor amplitudes and plume height reveals a striking hysteresis pattern. The tremor and plume height time series both show a gradual rise at the beginning of the eruption, but the plume height remains high and then declines rapidly at the end of the eruption (Fig. 3). The seismic and infrasonic (DLL only) amplitudes are plotted against plume height and are colored according to time, with tremor amplitudes being measured in the sampling window preceding the plume height observations (<5 minutes) (Fig. 4). During the initial, waxing portion of the eruption, the relationship between seismic and infrasonic amplitude and plume height is relatively constant. The decline of the eruption (after 16:45) reveals a different relationship, whereby the seismic and infrasonic tremor levels drop rapidly. Analysis of nearby radiosonde measurements from Cold Bay (60 km) indicates changes in the wind and

temperature structure would not substantially affect the tremor and plume height relationship.

Similar clockwise hysteresis has been observed in comparisons of high frequency (>1 Hz) seismic noise from rivers and discharge derived from water level during storm events (e.g. *19, 20, 21*). At the beginning of the storm, the riverbed is armored and densely packed. The rising portion of the storm destroys this armor and sediment impact creates considerable seismicity. After the peak of the storm, the riverbed begins to reform to a densely packed state (*20*). Physical models (*22, 23*) and observations (e.g. *20*) suggest the source of seismic noise from rivers is related to both bedload transport and turbulent flow, with changes in sediment flux during a storm being the dominant cause of the hysteresis. Glacial discharge and seismic tremor also correlate and display hysteresis (*24*), suggesting this phenomenon may exist for a wide range of fluid flow processes.

We propose a similar conceptual model for the volcanic tremor hysteresis observed at Pavlof, wherein the seismic and acoustic tremor amplitude is closely linked to the state of the volcanic vent and the stage of the eruption (*6*). Prior to the March 2016 Pavlof eruption, the upper portion of the conduit was in a densely packed state, plugged with degassed magma. The eruption was likely fed by the rapid, primarily aseismic rise of fresh magma over a short period of time (2-3 days). During ascent, the magma decompressed and degassed, triggering explosive fragmentation. A high velocity flow of particles and gas eroded the conduit walls and vent, producing tremor and driving a jet of ash and gas into the atmosphere. The tremor amplitude showed a strong correlation with plume height during this waxing phase of eruption (stage 1), while extensive vent erosion was occurring. Once the vent was cleared, tremor amplitudes leveled off (stage 2) and

then decreased more rapidly in stage 3 as flow and particle impact against the vent walls diminished as the shallow conduit was already cleared and widened.

Multiple lines of evidence support our model. Before and after images from the eruption show extensive erosion of Pavlof's summit (Fig. S2). After the eruption, the entire summit crater was ~130 m wide and 110 m deep, compared to no well-defined crater prior to the eruption. The crater narrows down to a 30–40 m diameter, circular vent at the base. Using scaling relationships and plume height observations, we estimated the evolving vent radius during the first two stages of the eruption (Fig. 3C) (*13*). The vent widened rapidly at the beginning of the eruption and then stabilized, following a similar trend as the tremor amplitudes. The maximum estimated vent diameter is between 30–35 m, similar to that observed post-eruption. We infer that the low frequency seismic event originating near the summit at 16:45 signifies crater collapse or rapid widening, as this event corresponds to the inflection point in the hysteresis pattern (Fig. 4). Sudden vent widening induces magma fragmentation at shallower depths (*25*), potentially leading to enhanced bubble growth and ash production (*26*). Indeed, a major increase in volcanic lightning occurred around this time (Fig. 3C), supporting the idea of increased fine ash content in the volcanic plume (*27*). In stage 3, tremor amplitudes continue to decline, likely because the crater has sufficiently widened such that the erupting jet is no longer strongly coupled to the vent walls, thereby leading to a different relationship between tremor and plume height. Our proposed vent evolution is consistent with laboratory experiments of vent erosion, which show a rapid widening followed by stabilization and occasional sudden expansion (*28*).

Our findings are also consistent with the generic three-stage tremor model proposed by McNutt and Nishimura (*6*). Their analysis of tremor and conduit/vent features from 24 eruptions worldwide revealed that these stages represent the most common temporal evolution of eruption tremor. They found a gradual increase in tremor amplitude is common for the first eruption in a sequence of eruptions, perhaps due to the gradual breaking up and erosion of the conduit. After a leveling-off phase, an exponential decrease in tremor amplitude during the waning stage was observed in 92% of their examined eruptions (Fig. 3).

Comparison of the seismic and infrasonic tremor from Pavlof reveals a high similarity between amplitudes and temporal evolution, suggesting a linked seismo-acoustic source located within the shallow conduit or crater. These observations, along with the tremor and plume height hysteresis, guide our multi-stage conceptual model consistent with those from fluvial seismology and eruption observations from around the world. Future volcanic eruption monitoring and interpretations of volcanic tremor, including their relationship to plume height and eruption intensity, should take into account the stage of the eruption and state of the upper conduit and vent, as well as insight from other studies of flows and the vibrations they produce.

References and Notes:

1. S. De Angelis, D. Fee, M. Haney, D. Schneider, Detecting hidden volcanic explosions from Mt. Cleveland Volcano, Alaska with infrasound and ground-coupled airwaves. *Geophys. Res. Lett.* **39**, L21312 (2012).

2. C. F. Waythomas *et al.*, The 7–8 August 2008 eruption of Kasatochi Volcano, central Aleutian Islands, Alaska. *Journal of Geophysical Research: Solid Earth (1978–2012)* **115**, (2010).

3. D. Fee, R. S. Matoza, An overview of volcano infrasound: From hawaiian to plinian, local to global. *Journal of Volcanology and Geothermal Research* **249**, 123 (2013).

4. B. A. Chouet, R. S. Matoza, A multi-decadal view of seismic methods for detecting precursors of magma movement and eruption. *Journal of Volcanology and Geothermal Research* **252**, 108 (2013).

5. S. G. Prejean, E. E. Brodsky, Volcanic plume height measured by seismic waves based on a mechanical model. *Journal of Geophysical Research: Solid Earth* **116**, B01306 (2011).

6 S. R. McNutt, T. Nishimura, Volcanic tremor during eruptions: Temporal characteristics, scaling and constraints on conduit size and processes. *Journal of Volcanology and Geothermal Research* **178**, 10 (Nov, 2008).

7. A. M. Jellinek, D. Bercovici, Seismic tremors and magma wagging during explosive volcanism. *Nature* **470**, 522 (2011).

8. R. S. Matoza *et al.*, Infrasonic jet noise from volcanic eruptions. *Geophys. Res. Lett.* **36**, (APR 18 2009, 2009).

9. H. Kanamori, J. Mori, D. G. Harkrider, Excitation of atmospheric oscillations by volcanic eruptions. *Journal of Geophysical Research-Solid Earth* **99**, 21947 (Nov, 1994).

10. S. R. McNutt, Volcanic tremor amplitude correlated with the volcano explosivity index and its potential use in determining ash hazards to aviation. *Acta Vulcanol.* **5**, 193 (1994).

11. D. Fee, M. Garces, A. Steffke, Infrasound from Tungurahua Volcano 2006–2008: Strombolian to Plinian eruptive activity. *J. Volcanol. Geotherm. Res.* **193**, 67 (2010).

12. M. Ripepe *et al.*, Ash-plume dynamics and eruption source parameters by infrasound and thermal imagery: The 2010 Eyjafjallajökull eruption. *Earth and Planetary Science Letters* **366**, 112 (3/15/, 2013).

13. Materials and Methods are available as Supplementary Material on Science Online.

14. R. S. J. Sparks *et al.*, *Volcanic Plumes*. (John Wiley and Sons, New York, 1997), pp. 574.

15. L. G. Mastin *et al.*, A multidisciplinary effort to assign realistic source parameters to models of volcanic ash-cloud transport and dispersion during eruptions. *Journal Of Volcanology And Geothermal Research* **186**, 10 (Sep 30, 2009).

16. M. Ichihara, M. Takeo, A. Yokoo, J. Oikawa, T. Ohminato, Monitoring volcanic activity using correlation patterns between infrasound and ground motion. *Geophys. Res. Lett.* **39**, L04304 (2012).

17. R. S. Matoza, D. Fee, Infrasonic component of volcano-seismic eruption tremor. *Geophys. Res. Lett.* **41**, 2014GL059301 (2014).

18. K. T. Walker *et al.*, Source location of the 19 February 2008 Oregon bolide using seismic networks and infrasound arrays. *Journal of Geophysical Research: Solid Earth (1978–2012)* **115**, (2010).

19. A. Burtin, L. Bollinger, J. Vergne, R. Cattin, J. Nábělek, Spectral analysis of seismic noise induced by rivers: A new tool to monitor spatiotemporal changes in stream hydrodynamics. *Journal of Geophysical Research: Solid Earth* **113**, (2008).

20. L. Hsu, N. J. Finnegan, E. E. Brodsky, A seismic signature of river bedload transport during storm events. *Geophys. Res. Lett.* **38**, (2011).

21. D. L. Roth *et al.*, Migration of a coarse fluvial sediment pulse detected by hysteresis in bedload generated seismic waves. *Earth and Planetary Science Letters* **404**, 144 (10/15/, 2014).

22. V. C. Tsai, B. Minchew, M. P. Lamb, J. P. Ampuero, A physical model for seismic noise generation from sediment transport in rivers. *Geophys. Res. Lett.* **39**, (2012).

23. F. Gimbert, V. C. Tsai, M. P. Lamb, A physical model for seismic noise generation by turbulent flow in rivers. *Journal of Geophysical Research: Earth Surface* **119**, 2209 (2014).

24. T. C. Bartholomaus *et al.*, Subglacial discharge at tidewater glaciers revealed by seismic tremor. *Geophys. Res. Lett.* **42**, 6391 (2015).

25. L. G. Mastin, Insights into volcanic conduit flow from an open-source numerical model. *Geochemistry, Geophysics, Geosystems* **3**, 1 (2002).

26. C. Klug, K. V. Cashman, Permeability development in vesiculating magmas: implications for fragmentation. *Bulletin of Volcanology* **58**, 87 (1996).

27. C. Cimarelli, M. Alatorre-Ibargüengoitia, U. Kueppers, B. Scheu, D. B. Dingwell, Experimental generation of volcanic lightning. *Geology* **42**, 79 (2014).

28. S. A. Solovitz, D. E. Ogden, D. Kim, S. Y. Kim, Coupled fluid and solid evolution in analogue volcanic vents. *Journal of Geophysical Research: Solid Earth* **119**, 5342 (2014).

29. M. Beyreuther *et al.*, ObsPy: A Python toolbox for seismology. *Seismological Research Letters* **81**, 530 (2010).

30. C. A. Rowe, R. C. Aster, B. Borchers, C. J. Young, An automatic, adaptive algorithm for refining phase picks in large seismic data sets. *B Seismol Soc Am* **92**, 1660 (2002).

31. J. V. Olson, Noise suppression using data-adaptive polarization filters: Applications to infrasonic array data. *The Journal of the Acoustical Society of America* **72**, 1456 (1982).

32. M. Hutchins, R. Holzworth, J. Brundell, C. Rodger, Relative detection efficiency of the world wide lightning location network. *Radio Science* **47**, (2012).

33. D. Carbone, L. Zuccarello, A. Messina, S. Scollo, H. Rymer, Balancing bulk gas accumulation and gas output before and during lava fountaining episodes at Mt. Etna. *Scientific reports* **5**, (2015).

34. D. P. Drob, J. M. Picone, M. Garces, Global morphology of infrasound propagation. *Journal of Geophysical Research-Atmospheres* **108**, (Nov, 2003).

35. D. P. Drob *et al.*, An empirical model of the Earth's horizontal wind fields: HWM07. *Journal of Geophysical Research-Space Physics* **113, A12304**, (Dec, 2008).

36. J. M. Picone, A. E. Hedin, D. P. Drob, A. C. Aikin, NRLMSISE-00 empirical model of the atmosphere: Statistical comparisons and scientific issues. *Journal of Geophysical Research-Space Physics* **107**, (Dec, 2002).

37. P. Blom, GeoAc: Numerical Tools to Model Acoustic Propagation in the Geometric Limit. *Los Alamos National Laboratory*, (2014).

Acknowledgments: We thank P. Dawson and V. Tsai for early reviews of the manuscript; C. Szuberla for discussions on signal processing; R. Wessels and M. Kaufman for imagery of Pavlof before and after the eruption; H. Schwaiger for the atmospheric modeling; and the reviewers and Associate Editor for their helpful comments. Seismic and EarthScope TA data are available from the Incorporated Research Institutions for Seismology Data Center (www.iris.edu). Observations of volcanic activity were made by AVO and are detailed on its website (www.avo.alaska.edu). Webcam data are available from the FAA Aviation Weather Cameras website (http://avcams.faa.gov). DLL infrasound data are available from D. Fee and the Wilson Alaska Technical Center. The World Wide Lightning Location Network (http://wwlln.net) provided the lightning data. The authors acknowledge support from the Alaska Volcano Observatory and NSF Grants EAR-1331084, EAR-1614323, and EAR-1614855. A. Van Eaton acknowledges a U.S. Geological Survey Mendenhall Fellowship.

Figure Captions:

Fig. 1. Map of Pavlof Volcano and seismic and infrasound stations in the region. A) Map of Alaska showing Pavlof (red triangle), the DLL and IS53 infrasound arrays (blue diamonds), and TA stations (black squares). Filled squares denote the four TA stations that recorded the eruption. B) Map of Pavlof Volcano, with the volcano's summit denoted by a red triangle. The six AVO seismic stations are marked with black squares.

Fig. 2. Seismo-acoustic coherence analysis for TA station O19K. A) Infrasound and B) seismic waveforms during the eruption filtered in the band 0.8-5 Hz. C) Windowed seismo-acoustic coherence has high values between ~05:00-20:00, indicating coherent acoustic waves on the infrasound and seismic channels. D) Coherence-weighted infrasound waveform. E) Filtered waveform from the local seismic station (PS1A) for comparison.

Fig. 3. Volcanic tremor, ash plume observations, and estimates of vent radius. Shading denotes the three stages of eruption described in text. A) Seismic (black-PS1A) and infrasonic (red solid-DLL and red dashed-O19K) envelopes during the Pavlof eruption. Infrasonic data are corrected for travel time. Star indicates low frequency seismic event at 16:45. B) Plume heights measured from webcam (daylight hours only) and satellite imagery. C) Vent radius calculated as a function of time (black dots) for stages 1 and 2, and volcanic lightning detections.

Fig. 4. Tremor amplitudes compared to plume height as a function of time. A) Seismic and B) infrasound amplitudes are plotted against the corresponding plume height, and are colored as a function of time. Two distinct relationships are present and correspond to the waxing and waning portions of the eruptions and changing source conditions. The clockwise hysteresis is indicated by the two arrows. Error bars for the satellite plume heights are determined using different pixel averaging techniques.

Supplementary Materials:

Materials and Methods

Figures S1-S2

References (29-37)

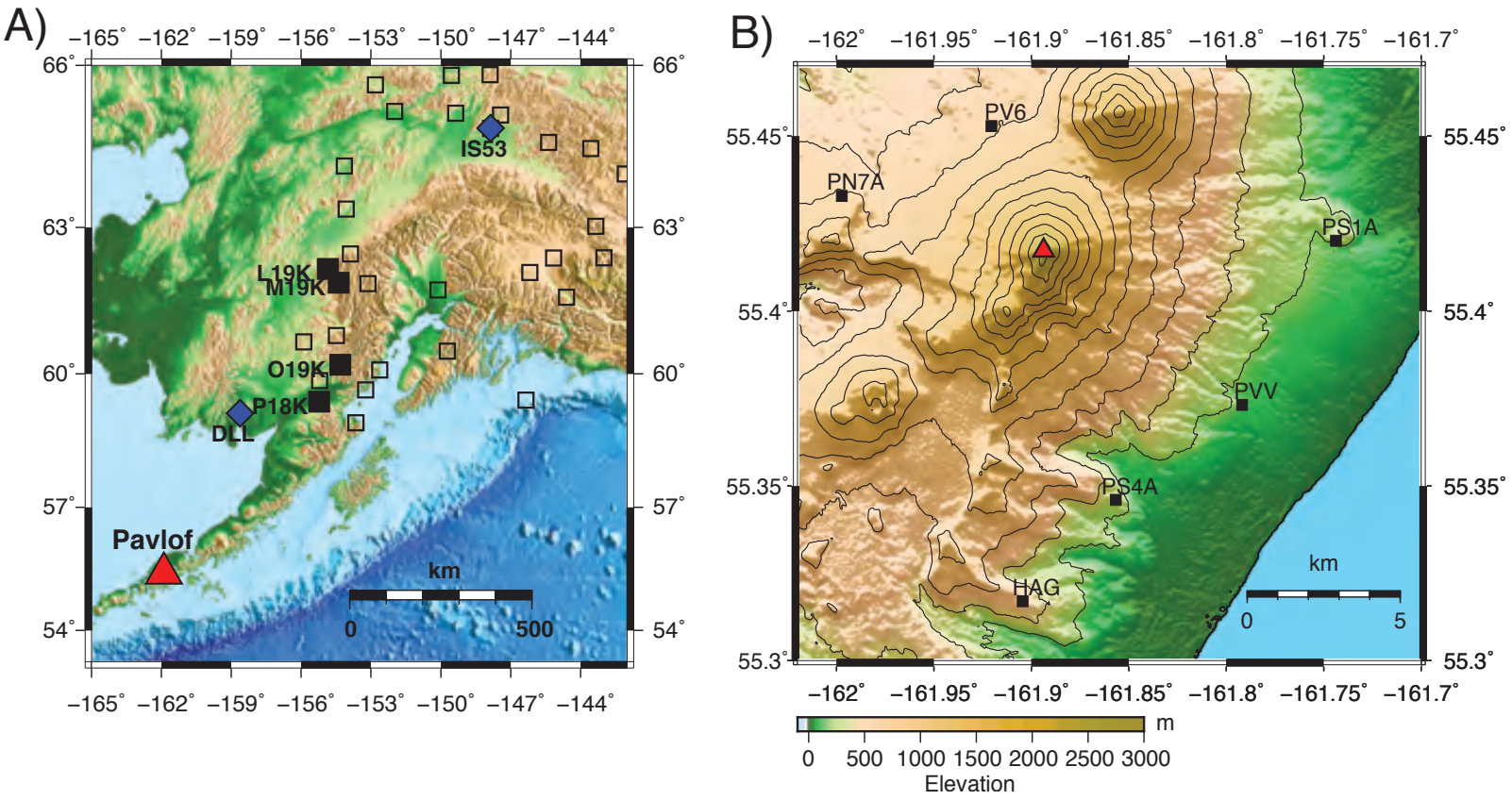
A)
−165° −162° −159° −156° −153° −150° −147° −144°
66°
63°
60°
57°
54°
IS53
L19K
M19K
O19K
P18K
DLL
Pavlof
km
0
500
B)
−162° −161.95° −161.9° −161.85° −161.8° −161.75° −161.7°
55.45°
55.4°
55.35°
55.3°
PV6
PN7A
PS1A
PVV
PS4A
HAG
km
0
5
m
0 500 1000 1500 2000 2500 3000
Elevation

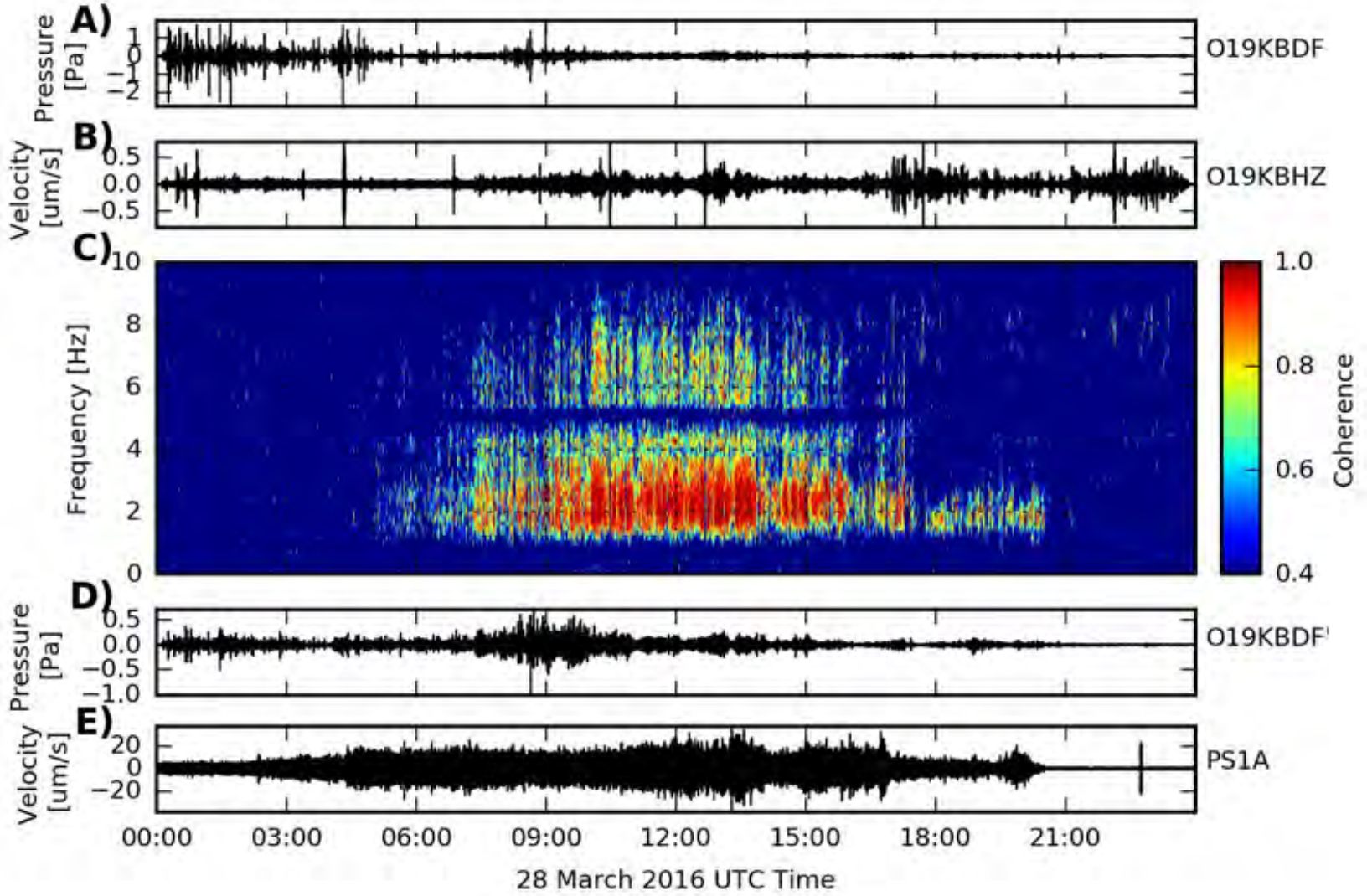
A)
Pressure [Pa]
1
0
−1
−2
O19KBDF
B)
Velocity [um/s]
0.5
0.0
−0.5
O19KBHZ
C)
Frequency [Hz]
10
8
6
4
2
0
1.0
0.8
0.6
0.4
Coherence
D)
Pressure [Pa]
0.5
0.0
−0.5
−1.0
O19KBDF
E)
Velocity [um/s]
20
0
−20
PS1A
00:00
03:00
06:00
09:00
12:00
15:00
18:00
21:00
28 March 2016 UTC Time

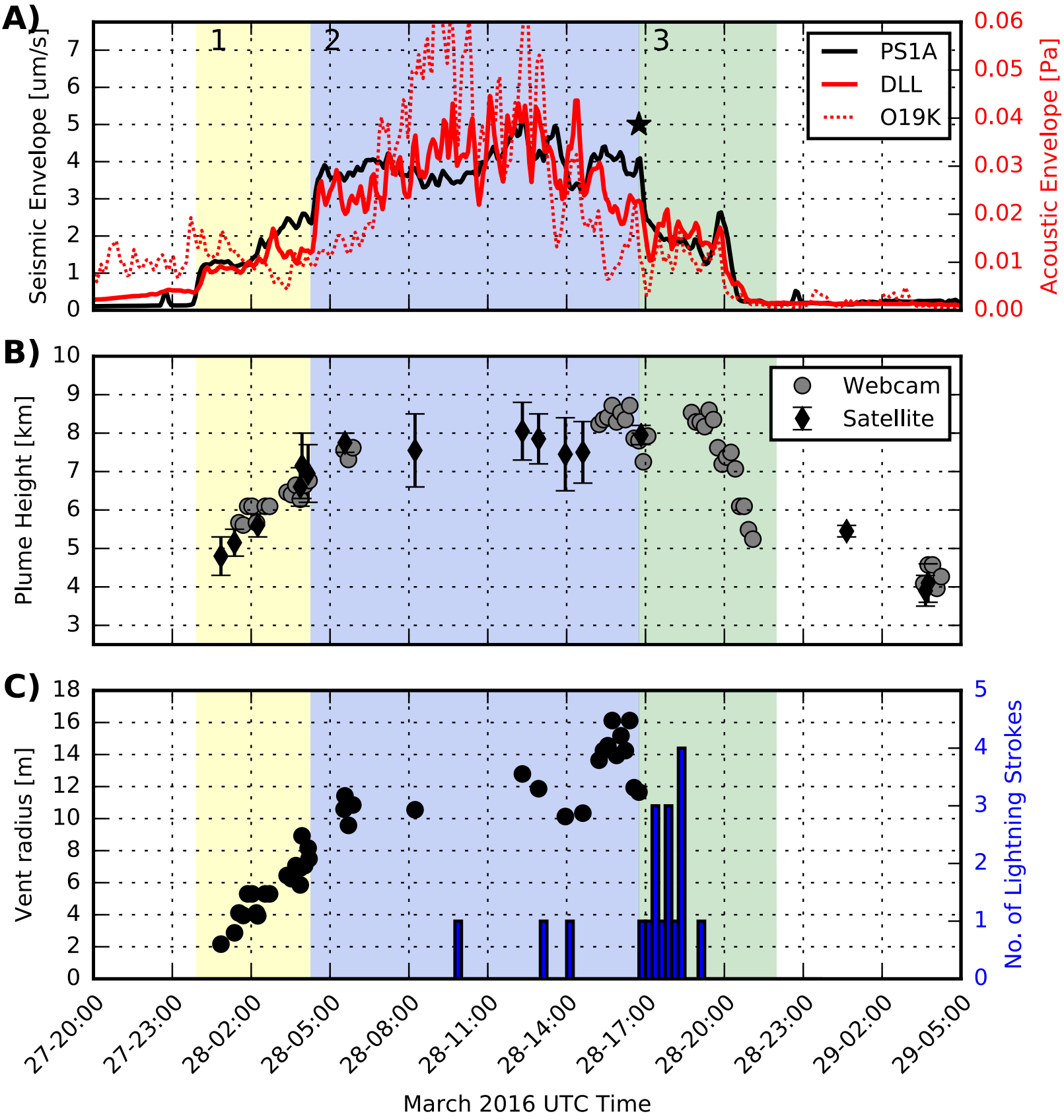
A)
B)
C)
1
2
3
PS1A
DLL
O19K
Seismic Envelope [um/s]
Acoustic Envelope [Pa]
Webcam
Satellite
Plume Height [km]
Vent radius [m]
No. of Lightning Strokes
27-20:00
27-23:00
28-02:00
28-05:00
28-08:00
28-11:00
28-14:00
28-17:00
28-20:00
28-23:00
29-02:00
29-05:00
March 2016 UTC Time

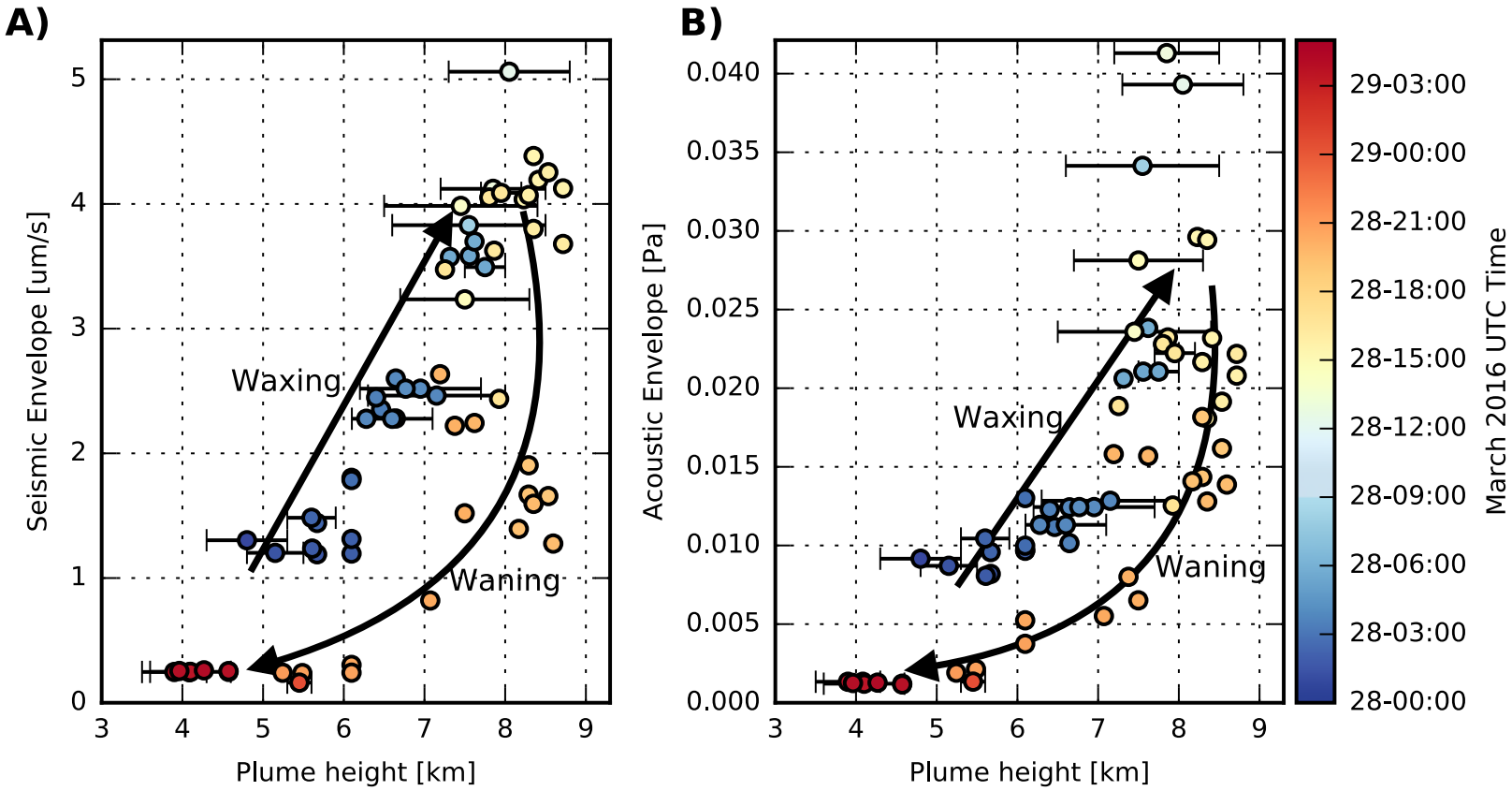
A)
B)
Seismic Envelope [um/s]
Acoustic Envelope [Pa]
Plume height [km]
Plume height [km]
Waxing
Waning
Waxing
Waning
March 2016 UTC Time
29-03:00
29-00:00
28-21:00
28-18:00
28-15:00
28-12:00
28-09:00
28-06:00
28-03:00
28-00:00

Supplementary Materials:

Materials and Methods

Waveform Data Analysis

Seismic and acoustic data were analyzed in part using ObsPy (*29*). Local seismic data consists of short-period (1 Hz) seismometers recorded at 100 Hz. Seismic data from the Alaska Volcano Observatory station PS1A were analyzed, and the instrument response was removed. Station PN7A was non-functional before the eruption and PV6 was destroyed during the eruption. Data from stations PV, PS4A, and HAG shows similar trends to PS1A, but clip during the energetic portions of the eruption. DLL consists of six infrasound elements spread over 1.2 km at a distance of 460 km from Pavlof. Infrasound array data from DLL were processed using a standard delay-and-sum beamforming technique to increase the SNR. A local infrasound sensor at station PN7A was also non-functional prior to the eruption. Infrasound and seismic data were filtered between 0.8-5 Hz using a 4-pole, acausal Butterworth filter. The envelope functions were calculated by taking the analytic signal of the Hilbert transform and averaging over a 5-minute interval. A 5-point, convolutional filter is then applied to each envelope to smooth out small deviations.

Coherence-weighted filtering

We use a waveform filtering technique similar to coherency-filtering employed on large seismic data sets (*30*) and the Pure State Filter used on infrasound data (*31*). The seismic and acoustic time-series data from O19K, $w(t)$ and $p(t)$, are divided into 30 s time segments with 27 s overlap. The coherence (magnitude-squared coherence), C_{xy}, is calculated between the two waveforms for each window. The acoustic data segments are Fourier transformed to produce $P(f)$. For each segment and discrete frequency, the square of the coherence is multiplied by $P(f)$, and then inverse Fourier transformed to produce a coherence-weighted acoustic time-series:

$$p'(t)=\mathrm{IDFT}[P(f)*C_{xy}^{2}] \qquad (1)$$

The square of the coherence is used to provide additional weight to coherent periods, as suggested by Olson (*31*). After this process incoherent frequency components in the acoustic data are suppressed significantly (Fig. 2). Data from station O19K was sampled at 40 Hz. Narrow spikes in some of the waveforms are short data glitches and occasional small earthquakes.

Plume heights and volcanic lightning

Webcam-derived plume heights are calculated by overlaying extrapolated altitudes on the webcam image, using the background topography as reference. Vertical pixel resolution is ~60 m. Satellite-derived plume heights are estimated using the plume top temperature method (e.g. *14*). The plume top is considered to be thermally equilibrated with the surrounding atmosphere. The upper bound on the plume height estimate (Fig. 3B,4) is determined by matching the coldest pixel from the thermal infrared satellite image with

the corresponding temperature from the Cold Bay radiosonde. The lower bound of the plume height is determined using the same technique, but estimates the plume top temperature by averaging a 5x5 pixel grid surrounding the coldest pixel. We used the average of minimum and maximum heights from the webcam and satellites to compare with seismic and infrasonic amplitudes. All plume heights are listed in km above sea level, and the summit of Pavlof is ~2.4 km.

Volcanic lightning was detected by the World Wide Lightning Location Network (http://wwlln.net). The WWLLN Volcanic Lightning Monitor provides publicly available lightning locations within 100 km of each active volcano. WWLLN determines lightning locations from the time of arrival of the very low frequency radio wave packets generated by lightning stroke currents, detected by five or more of the 80+ receiving stations globally (*32*). Timing precision is generally <10 μs and spatial accuracy is <5 km. All lightning detected within 20 km of Pavlof Volcano from 28–29 March 2016 can be assumed of volcanic origin based on the lack of meteorological storms during this time.

Volcanic vent radius estimation

The relationship between volcanic plume height and mass eruption rate has been derived empirically from measurements of well-documented modern eruptions by Mastin et al. (*15*):

$$M = 140 H_{obs}^{4.15} \qquad (2)$$

where H is the observed column height in km above the vent and M is the mass flux in kg/s. The mass flux of a pressure-adjusted, gas-pyroclast mixture exiting a circular vent can also be expressed as:

$$M = \pi r^2 \rho_B u \qquad (3)$$

where r is the vent radius in m, ρ_B is the bulk density of the pressure-adjusted jet, and u is the velocity of the erupted mixture. This assumes the erupted mixture has equilibrated to atmospheric pressure.

Although we do not have direct measurements of volcanic jet velocity, it can be estimated from the height of ballistic ejecta, which we estimate from the height of the incandescent fountain observed in the webcam (*33*):

$$u = \sqrt{2 g H_f} \qquad (4)$$

where H_f is the fountain height and g is the standard acceleration due to gravity. This assumes the particles are large enough that air resistance can be neglected. For Pavlof, the maximum fountain height was estimated to be around 700 m from analysis of nighttime webcam imagery, which corresponds to a particle velocity of 117 m/s.

Using Eqs. 2 and 3 we can solve for the vent radius (e.g. *12,33*):

$$r = \sqrt{\frac{140 H_{obs}^{4.15}}{\pi \rho_B u}} \qquad (5)$$

We assume a plume bulk density of 3 kg/m^3, which corresponds to an exsolved water content of ~5 wt%. Note the radius of the vent will scale with the square of the plume height if the bulk density and velocity are held constant.

The vent radius is plotted in Figure 3C during stages 1 and 2 using our measured plume heights and assuming a constant bulk density and vent velocity as described above. We infer that the start of stage 3 (16:45 UTC) represents a regime shift in the vent system, after which the scaling analysis no longer applies. Beyond this point, we infer that the particle-laden eruptive jet no longer coupled strongly to the vent walls.

Acoustic propagation

The acoustic propagation time from Pavlof to DLL (460 km distance) is calculated using ray tracing with relevant atmospheric specifications, and is removed to allow comparison with the local seismic data. The acoustic travel time is 1357 s. Atmospheric specifications are assembled following the method of Drob et al. (*34*). Tropospheric conditions are available as forecasts using the GFS (Global Forecast System) model from NCEP (National Centers for Environmental Prediction), which provides 3-hourly forecasts of conditions from the surface to a pressure level of 10 mbar (approximately 35 km in altitude) at a spatial resolution of 0.5-degrees. Mesospheric and thermospheric values were calculated using the HWM07 model (*35*) for winds, and the NRLMSISE-00 (*36*) for temperatures. These upper atmospheric empirical models require knowledge of two solar-terrestrial indices (F107 and Ap.) Current values are available from the NOAA Space Weather Prediction Center.

Rays are calculated between Pavlof's summit and DLL and O19K using the GeoAc software distribution (*37*). Rays are propagated out from the summit of Pavlof at angles of -30 to 45 degrees from horizontal. The ray that best connects the source with the receiver is selected, and the travel time is then removed. An acoustic travel time of 1,357 seconds is calculated for DLL and sound was predicted to propagate predominantly in a tropospheric waveguide. Propagation conditions between Pavlof and DLL do not change significantly during the eruption, so a range-independent assumption was made. Atmospheric specifications are constructed using a similar methodology to the NRL-G2S specifications (*34*) by integrating high-resolution lower atmosphere model data with upper atmosphere climatological models. Our results and model are not critically dependent on changes in acoustic propagation time.

Supplementary Figures

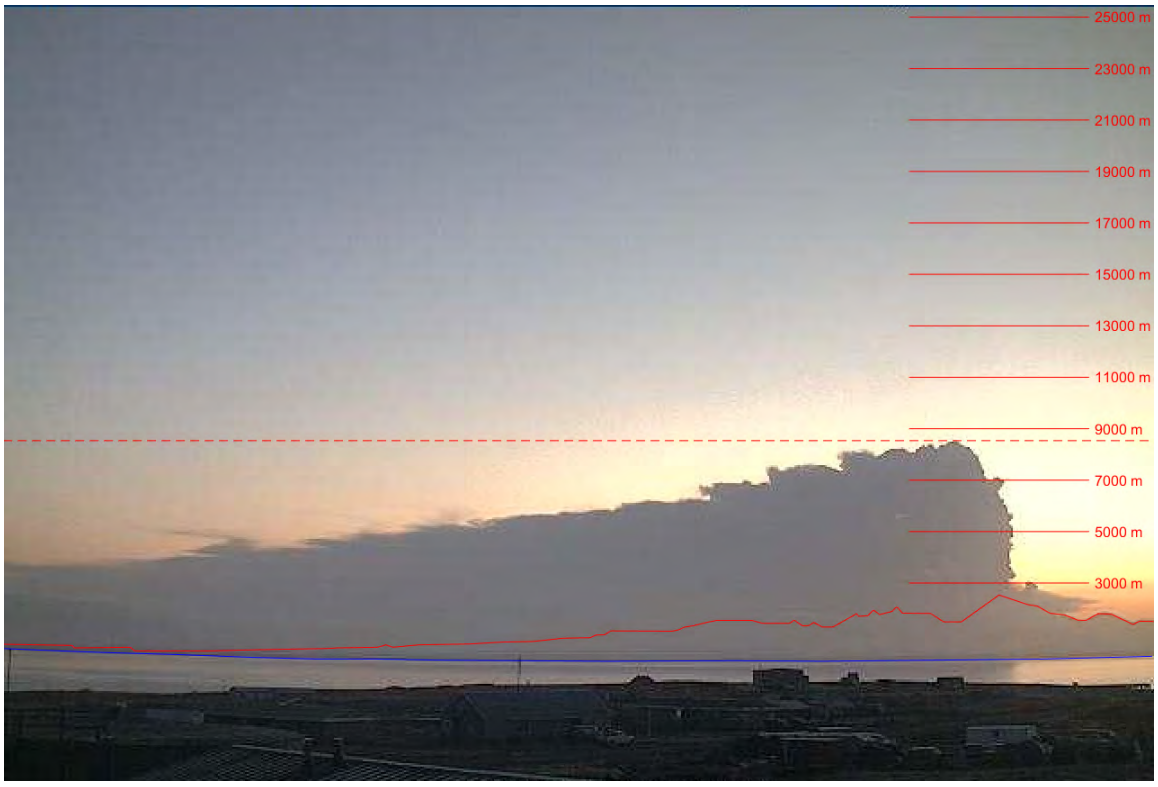

Fig. S1. Webcam image of the Pavlof plume on 28 March 16:04 UTC, with topography and extrapolated height above the vent overlain.

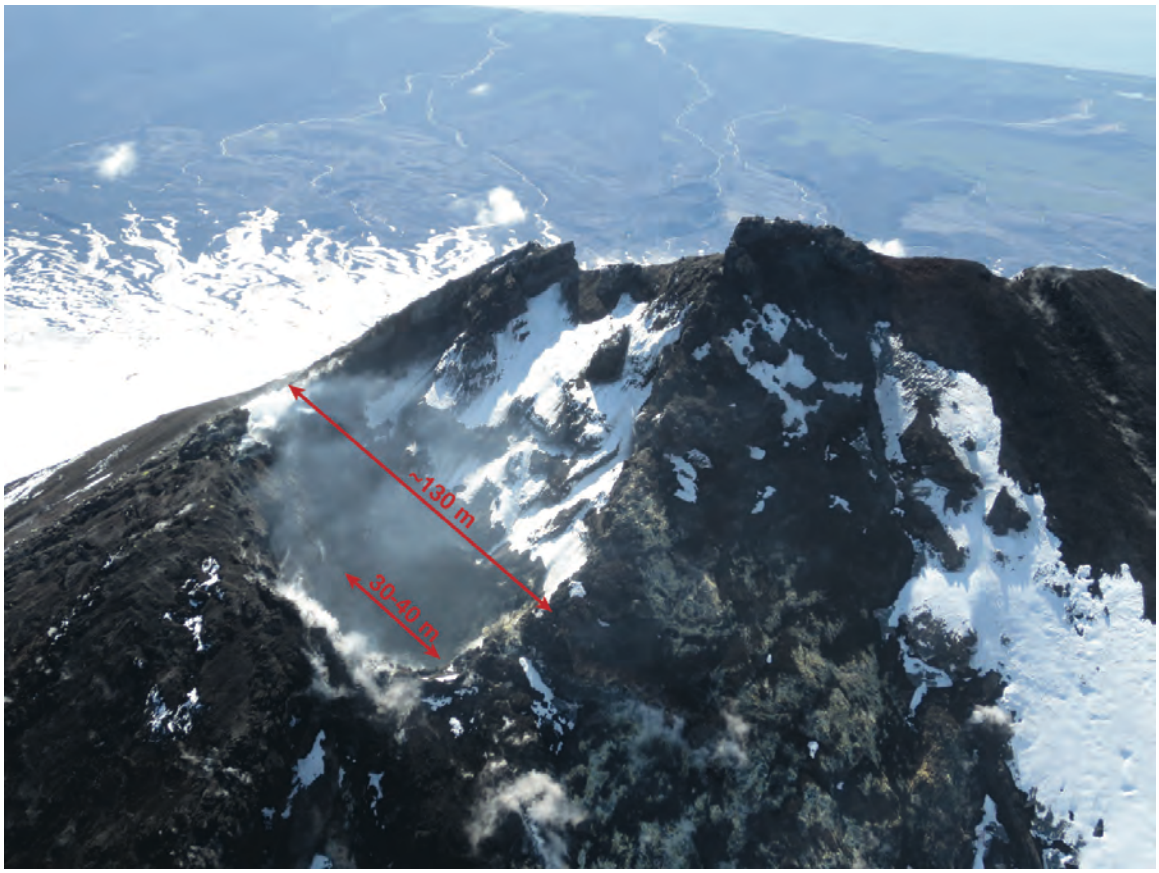

Fig. S2. Photograph of Pavlof's summit taken after the eruption. The crater and upper conduit have been heavily eroded, consistent with our proposed model. Although no clear, high-resolution images of the summit were made before the eruption, no noticeable crater was observed. Post-eruption estimates of the crater are ~130 m diameter and 110 m deep with a well-defined vent at the base of the crater of 30-40 m. Photo by Max Kaufman (University of Alaska Fairbanks/AVO) taken on 7 June 2016, and crater size estimates courtesy of Rick Wessels (USGS).